ROBUST DESIGN OF NEGATIVE STIFFNESS ELEMENTS FABRICATED BY SELECTIVE LASER SINTERING

David Shahan, Ben Fulcher, Carolyn Conner Seepersad,
Michael R. Haberman, Preston S.Wilson

Mechanical Engineering Department
University of Texas at Austin, Austin, TX, 78712

Abstract

Constrained negative stiffness structures have been shown to possess desirable vibration isolation properties because of their ability to provide low dynamic stiffness, resulting in low transmissibility over a wide range of frequencies. In this research, selective laser sintering (SLS) is an integral part of a model-design-build-test process for investigating the vibration isolation capabilities of negative stiffness structures in the form of axially compressed beams. SLS provides geometric design freedom and rapid fabrication capabilities for validating dynamic models of structural behavior and guiding the design process toward iterative improvements. SLS also introduces some geometric and dimensional variability that can significantly degrade the performance of the structure. In this paper, an iterative model-design-build-test process for negative stiffness structures is described and presented with an analysis of the impact of SLS-induced imperfections on the results.

1. Introduction

To motivate the use of negative stiffness elements for the purposes of vibration isolation, consider the lumped parameter mass-spring-damper system shown in Figure 1. Minimizing the transmissibility of the base excitation to the supported mass can be achieved through a near zero combined spring stiffness. However, a single weak spring will not be able to support a static load. If a positive stiffness spring, k_{pos}, is used to support the mass then a static deflection will occur until the weight is balanced by the spring force. If a negative stiffness spring, k_{neg}, is added in parallel, then the total system dynamic stiffness can theoretically be reduced to near zero while still statically supporting the mass. The system's dynamics can be explained by Equation 1 with the associated transfer function of Equation 2 (Blake, 2010). Figure 2 plots the transmissibility due to a sinusoidal base displacement for different values of negative stiffness for a fixed positive stiffness. The isolation is more effective at near zero total system dynamic stiffness, also known as quasi-zero stiffness (Alabuzhev et al, 1989).

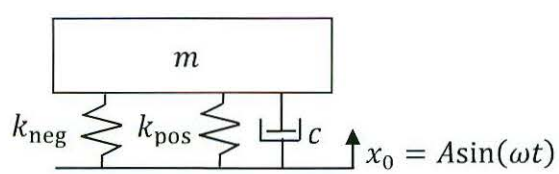

Figure 1. Mass-Spring-Damper Base Isolation System

$$m\ddot{x} + c\dot{x} + (k_{\text{pos}} + k_{\text{neg}})x = c\dot{x}_0 + (k_{\text{pos}} + k_{\text{neg}})x_0 \tag{1}$$

$$|H| = \sqrt{\frac{1 + \left(\frac{c\omega}{k_{\text{pos}} + k_{\text{neg}}}\right)^2}{\left(1 - \frac{m\omega^2}{k_{\text{pos}} + k_{\text{neg}}}\right)^2 + \left(\frac{c\omega}{k_{\text{pos}} + k_{\text{neg}}}\right)^2}} \quad (2)$$

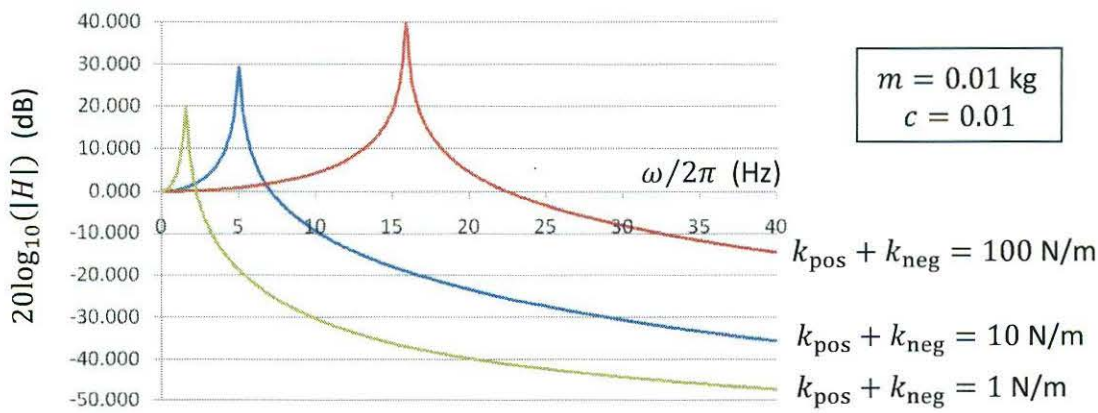

Figure 2. Transmissibility of Mass-Spring-Damper Base Isolation System

Previous research validated the concept of using the negative stiffness behavior of axially compressed beams for vibration isolation (Kashdan et al., 2011). To the best of the authors' knowledge, this research effort was the first to produce negative stiffness vibration isolation with additive manufacturing capabilities. In this paper, prior work is extended by providing a more detailed model of the behavior of negative stiffness beams, describing its validation with SLS prototypes, and investigating the role of manufacturing-induced imperfections in the model-design-build-test process.

The paper is organized according to the following outline. In the next section we develop a model for analyzing negative stiffness using an axially compressed beam. In Section 3, a system-level dynamic model is developed using the results from Section 2 and compared to the performance of an SLS prototype. Part of the discrepancy between the experimental data and the model-based predictions is attributed to manufacturing-related variability in the prototype, and its impact is quantified in Section 4. Section 5 concludes with a discussion of the results and directions for future work.

2. Modeling an Axially Compressed Beam as a Negative Stiffness Element

Negative stiffness can be achieved by axially compressing a beam beyond its first-mode-buckling limit. Consider the horizontally oriented, fixed-end rectangular beam shown in Figure 3. When the beam is axially compressed by a load P, its transverse stiffness at the midpoint, $k_{\text{b}} = F/u_{\text{y}}$, decreases according to Equation 3 (Young, 1989; Timoshenko and Gere, 1961).

$$k_{\text{b}} = \frac{192EI}{l^3}\frac{s^3}{3(\tan(s)-s)}, \quad s = \frac{l}{4}\sqrt{\frac{P}{EI}} \quad (3)$$

The beam's rectangular cross-section has an area moment of inertia, $I = wh^3/12$, and E is the elastic modulus of the beam material. Figure 4 plots the total system stiffness as a function of axial beam compression. The lowest curve corresponds to Equation 3 with the values for the beam height, width, and elastic modulus as shown in the box in the upper right corner of the figure. Notice that for low levels of axial compression, P, the beam alone has a positive stiffness. The compressive force at which the beam stiffness reaches zero is the first critical buckling load, P_{cr1}. The other curves correspond to total system stiffness with a positive stiffness k_{s} added in parallel with the beam stiffness. The additional stiffness k_{s} shifts the total system stiffness up and extends the zero-stiffness first-mode-buckling point to the right. The negative stiffness contribution of the beam to the total system stiffness is shown as a dashed line extending into the negative stiffness portion of the graph in Figure 4. The vertical red lines are the critical buckling loads, P_{cri}, for the first three buckling modes, $i = 1, 2, 3$, of the beam.

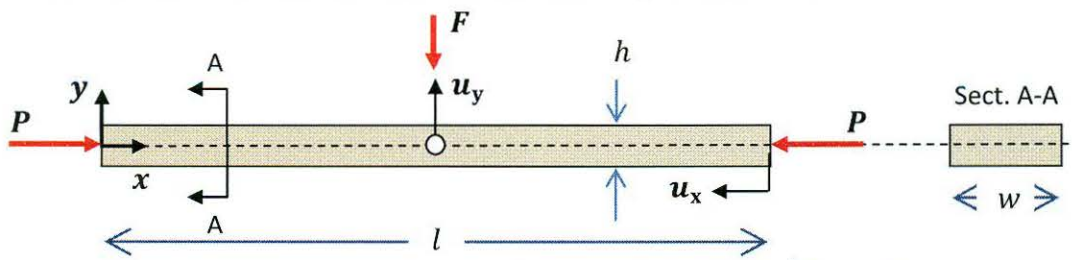

Figure 3. Axially Compressed Beam as a Negative Stiffness Element

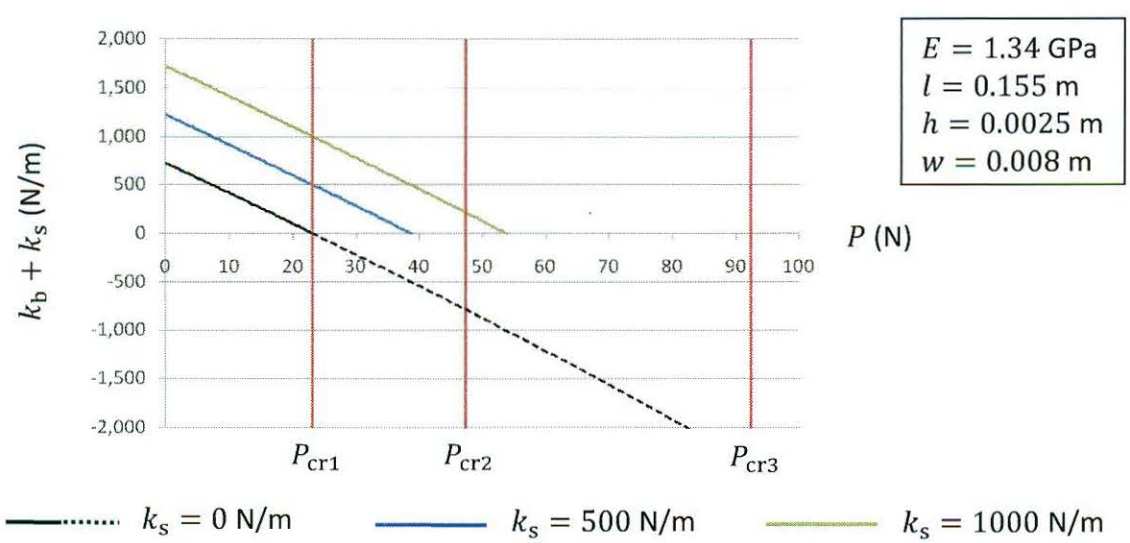

Figure 4. Transmissibility of Mass-Spring-Damper Base Isolation System

For a zero compressive load, the transverse beam stiffness, k_{b0}, is positive and quantified by Equation 4. As shown in Equation 5, which is related to Equation 3, the beam's stiffness decreases approximately linearly with k_{b0} as the axial compressive force increases. Using this linear approximation to the beam stiffness, the total system stiffness, k, can be expressed as Equation 6, in which the positive stiffness and negative stiffness are assumed to be isolated, and

the negative stiffness is a function of the ratio, α, of the axial compressive force on the beam to the first buckling critical load, P/P_{cr1}.

$$k_{\mathrm{b0}} = \frac{192EI}{l^3} \tag{4}$$

$$k_{\mathrm{b}} \approx k_{\mathrm{b0}}\left(1 - \frac{P}{P_{\mathrm{cr1}}}\right) \tag{5}$$

$$k = k_{\mathrm{pos}} + k_{\mathrm{neg}} \approx k_{\mathrm{s}} + k_{\mathrm{b0}} - k_{\mathrm{b0}}\alpha, \quad \alpha = \frac{P}{P_{\mathrm{cr1}}} \tag{6}$$

The amount of negative stiffness that an axially compressed beam can achieve is limited by buckling. The first three buckling mode shapes are shown in Figure 5, as calculated from Euler-Bernoulli buckling theory (Timoshenko and Gere, 1961). The midpoint deflection of the first-mode shape shown at the top of Figure 5 explains why first-mode buckling corresponds to zero midpoint stiffness. The axial load at which this buckling mode occurs can be increased by adding a spring at the beam's midpoint, constraining the midpoint from deflecting into the first-mode shape. This situation corresponds to the two curves in Figure 4 with nonzero stiffness, k_{s}. For example, for the k_{s} = 500 N/m curve in Figure 4 the new first-mode shape buckling load limit has been shifted from about 23 N to just under 40 N. However, constraining the vertical displacement of the beam's midpoint does not affect the second and third-mode shapes shown at the middle and bottom of Figure 5 respectively. If the beam's midpoint stiffness is increased such that the first-mode-buckling load is higher than the second-mode-buckling load and if the beam's midpoint is free to rotate, the beam will buckle into the second-mode as shown in the middle of Figure 5. This situation corresponds to the k_{s} = 1000 N/m curve in Figure 4, which will not extend to the zero stiffness axis if it is second-mode buckling limited, stopping instead at the vertical red line corresponding to the second-mode critical buckling load, P_{cr2}, of about 47 N. However, if the beam midpoint is rotationally constrained such that the second buckling mode will not occur, then it can be axially compressed to zero stiffness as long as it does not achieve axial strains corresponding to higher buckling loads first. This situation corresponds to the k_{s} = 1000 N/m curve in Figure 4 extending past the vertical red line of the second-mode critical buckling load and stopping at the zero stiffness axis at about 54 N, which is well below the third-mode critical buckling load of about 92 N.

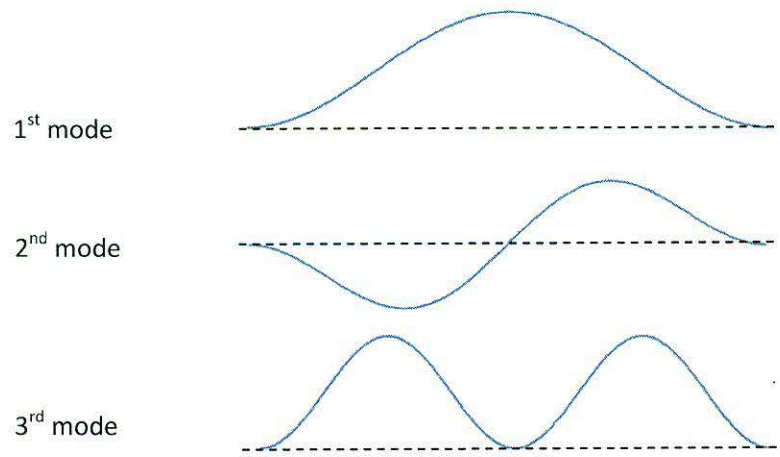

Figure 5. First Three Buckled Beam Mode Shapes

Buckling limits negative stiffness because, once buckled, it becomes very difficult to add additional compressive load into the beam. This effect is illustrated in Figure 6 where the axially compressive load P increases according to the slope AE/l as the distance between the beam's endpoints is decreased by u_x until it buckles at the critical load. The loads at which these buckling modes occur can be calculated using Equation 7 (Timoshenko and Gere, 1961).

$$P_{\mathrm{cri}} = \frac{4(\lambda_{\mathrm{i}})^2 EI}{l^2}, \lambda_{\mathrm{i}} = \pi, 4.493, 2\pi, 7.725 \ldots, i = 1, 2, 3, 4 \ldots \tag{7}$$

Once the beam has buckled, the load P no longer increases with additional movement of the beam endpoints toward each other; instead, all of the energy goes into bending the beam into its mode shape. These results were replicated in a finite element analysis by including an initial beam shape that is not perfectly straight but whose node locations along the beam's length follow the buckled mode shape multiplied by a scale factor. Thus the beam geometry is made imperfect with a predisposition to buckle into the predicted mode shape. When these beams are compressed, the reaction load follows the dashed lines in Figure 6. The larger the imperfection, the more gradual is the transition from axial compression to bending.

These results present the challenge of designing negative stiffness elements with compressed beams for use in quasi-zero stiffness vibration isolation. For low frequency isolation, the total system stiffness needs to be as close to zero as possible. For isolating large masses, a large positive stiffness will be required to support the static load and hence more negative stiffness is required to achieve low dynamic stiffness. However, the amount of negative stiffness that a beam can achieve is limited by buckling. Buckling is also dependent upon the amount of imperfection in the beam geometry and the boundary conditions. Before developing these design considerations further, the models are validated with experimental data from an SLS prototype system.

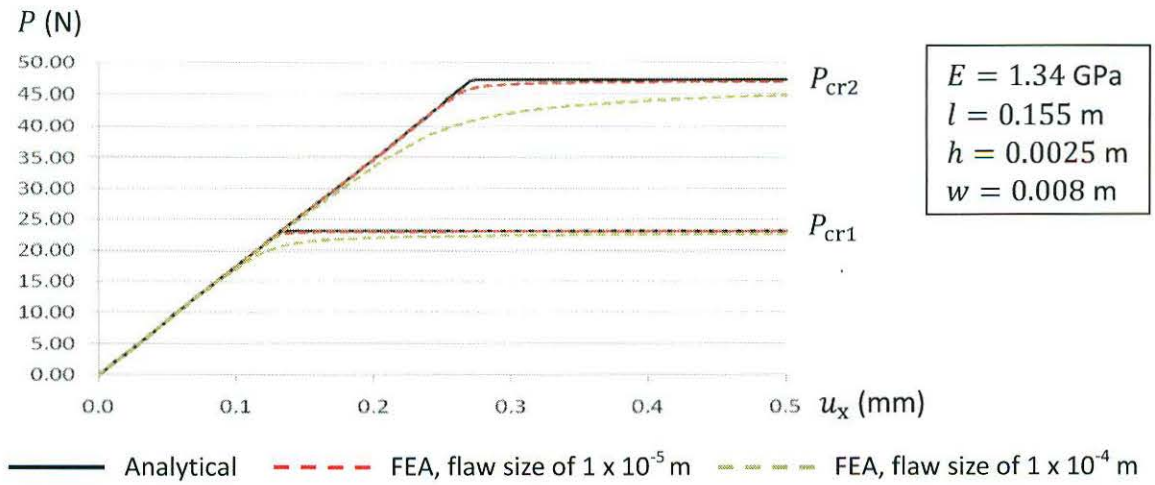

Figure 6. Axial Compression Load as a Function of the Decreasing Distance between the Beam Endpoints

3. System Dynamics Modeling and Prototype Testing

A simple prototype was designed to validate the models developed in the previous section. The goal of the test was to replicate the predicted transmissibility of the system as a function of axial preload. Figure 7 shows a picture of the prototype built with SLS out of Nylon 11. The prototype includes one sliding interface (the left face in Figure 7) that can be used to compress the horizontal beam, which is the negative stiffness element, by tightening nuts on the three threaded metal rods inserted into the system. During vibration testing, this sliding interface is fixed in place with screws visible at the lower left of the picture in Figure 7. The positive stiffness supporting spring was implemented as a helical coil spring connecting the base and the beam midpoint. With the exception of the threaded rods and set screws, the entire prototype was fabricated as one piece, thereby reducing the amount of extraneous noise in the system during dynamic testing. Testing the transmissibility of the prototype involved mounting it to a shaker table, placing an accelerometer at the beam midpoint to measure the system response and dividing the response by the output of an accelerometer placed on the base of the prototype. For this test the payload mass was the mass of the accelerometer, 0.0049 kg.

A complete characterization of the dynamics of this system requires models for the spring stiffness and the dynamic masses and damping of the beam and spring, in addition to the axial compression models developed in the previous section. The positive stiffness of the helical coil spring, k_s can be calculated from the coil diameter, D, the wire diameter, d, the number of active coils, N, and the shear modulus, G, according to Equation (8) (Juvinall and Marshek, 2000).

$$k_s = \frac{Gd^3}{8ND^4} \tag{8}$$

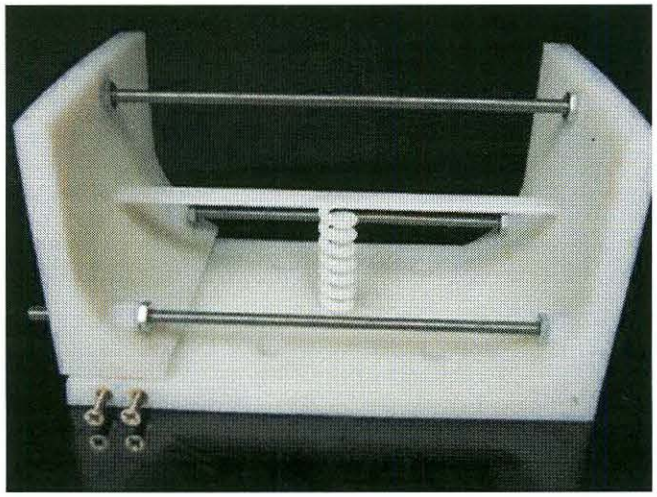

Figure 7. SLS Prototype for Axially Compressed Beam Vibration Isolation (Kashdan, 2010)

The dynamic mass of the beam can be estimated by equating the formula for the natural frequency of a fixed-fixed beam, ω_n, to the equivalent formula for a lumped parameter system, as shown in Equation 9 (Blevins, 1979). Equation 10 represents the beam mass fraction, μ, obtained by substituting Equation 4 for the beam's stiffness into Equation 9. The beam's dynamic mass is calculated by multiplying the mass fraction by the mass of the beam, m_b.

$$\omega_{\mathrm{n}} = \left(\frac{4.73}{l}\right)^2 \sqrt{\frac{EIl}{m_{\mathrm{b}}}} = \sqrt{\frac{k_{\mathrm{b}}}{\mu m_{\mathrm{b}}}} \tag{9}$$

$$\mu = \left(\frac{1}{4.73}\right)^4 \frac{k_{\mathrm{b}} l^3}{EI} = 192\left(\frac{1}{4.73}\right)^4 \cong 0.384 \tag{10}$$

The dynamic mass of the helical spring is one-third of its total mass, m_s, which can be calculated with Equation 11. The total dynamic mass of the system can be expressed as Equation 12, in which the payload mass is captured as m_{pl}.

$$m_{\mathrm{s}} = \rho_s \pi^2 N D d^2/4 \tag{11}$$

$$m = 0.384 m_{\mathrm{b}} + (1/3) m_{\mathrm{s}} + m_{\mathrm{pl}} = 0.384 \rho_{\mathrm{b}} whl + (1/12)\rho_s \pi^2 N D d^2 + m_{\mathrm{pl}} \tag{12}$$

With these expressions, the natural frequency of the system can be calculated from Equation 13 as a function of the axial beam load.

$$\omega_{\mathrm{n}} = \sqrt{\frac{k}{m}} = \sqrt{\frac{k_{\mathrm{s}} + k_{\mathrm{b0}} - k_{\mathrm{b0}}\alpha}{0.384 m_{\mathrm{b}} + (1/3) m_{\mathrm{s}} + m_{\mathrm{pl}}}} \tag{13}$$

This result was verified with a dynamic finite element model in the commercially-available software package Abaqus. The beam was modeled using 80 linear Timonshenko beam elements; the payload mass plus one-third of the spring mass was captured by a lumped mass element at the beam's midpoint node; and the supporting spring stiffness was captured with a linear spring element. The model parameters were selected to match the prototype's design parameters as documented in Table 1. Table 2 compares the analytical model results for the system natural frequency on the second row to the finite element results on the last row for the preload strains on the first row. The agreement is very good. For this set of parameters, the beam is expected to buckle into the second mode at 0.27 mm of compression. This explains the rapid decrease of resonant frequency through 0.26 mm of axial compression, followed by very little change in resonant frequency with further compression because the beam is buckled.

Table 1. Model Parameters

E, elastic modulus (GPa)	1.349
l, beam length (m)	0.155
w, beam width (m)	0.008
h, beam height (m)	0.0025
k_s, spring stiffness (N/m)	1319
m_{pl}, payload mass (kg)	0.0049

Table 2. Analytical and FEA Predicted Resonant Frequencies

Axial compressive displacement, u_x (mm)	0	0.13	0.26	0.40
Analytical resonant frequency, ω_n (Hz)	87.2	70.5	47.3	44.6
FEA resonant frequency, ω_n (Hz)	87.9	70.9	47.9	45.3

The primary source of damping in the prototype is due to the viscoelastic behavior of Nylon 11 which is well represented with an equivalent frequency dependent viscous damper as shown in Equation 14 (Blake, 2010). The material loss factor is represented by η and was measured in previous experiments to be 0.03 (Kashdan, 2010). The majority of the damping was assumed to occur in the vertical supporting spring. Based on these equations, the system's transfer function is represented by Equation 15.

$$c = \frac{\eta k}{\omega} = \frac{\eta k_s}{\omega} \tag{14}$$

$$|H| = \sqrt{\frac{1+\left(\eta\frac{k_s}{k}\right)^2}{\left(1-\left(\frac{\omega}{\omega_n}\right)^2\right)^2+\left(\eta\frac{k_s}{k}\right)^2}}, \; k = k_s + k_{b0} - k_{b0}\alpha \tag{15}$$

When building a prototype using SLS, there is substantial uncertainty in the fabricated material properties and dimensions due to variability in the manufacturing process. For this reason, validation of the analytical model requires statistical characterization of the post-build material properties and geometry. A standard rectangular tensile test specimen was included in the build to measure the elastic modulus of the sintered Nylon 11. Another tensile test specimen

was built with identical pre-build geometry as the helical coil spring for a closer estimate of the supporting spring stiffness. The primary dimensions of the negative stiffness beam were also measured with calipers. Each measurement was repeated six times. The data from these measurements is recorded in Table 3 along with the resulting means and standard deviations. The mean values can then be used in Equation 15 to provide a comparison to the transmissibility data obtained from the prototype.

Table 3. Parameter Measurements, Mean and Standard Deviations

	Trial 1	Trial 2	Trial 3	Trial 4	Trial 5	Trail 6	mean	standard deviation
E (GPa)	1.425	1.388	1.320	1.367	1.315	1.280	1.349	5.361×10^{7}
w (m)	0.00851	0.00843	0.00854	0.00849	0.00845	0.00850	0.00849	4.033×10^{-5}
h (m)	0.00287	0.00294	0.00290	0.00293	0.00291	0.00292	0.00291	2.483×10^{-5}
k_s (N/m)	1316	1263	1302	1334	1321	1381	1319	38.7

The experimental transmissibility data from this prototype are shown as solid lines in Figure 8, overlaid with the dashed lines of the model's prediction for several axial compression displacements. The first thing to notice about the transmissibility data is that it has the correct trend of a lower resonant frequency with increased axial compression. The second thing to notice is that the final axial compression did not lower the resonant frequency. The most likely explanation is that the beam buckled into its second-mode shape prematurely. In fact, using the mean values for the parameters in Table 3, the model predicts that the system will reach zero stiffness before buckling into the second mode. However, the premature buckling is not surprising considering that any geometric deviation from a perfectly straight beam with perfectly applied boundary conditions will encourage buckling before the analytical prediction. Finally, there was a large discrepancy between the predicted and observed shift in resonant frequency for the reported levels of compression. The most likely explanation for this discrepancy is inaccuracy in determining the amount of compression in the beam by counting the fractional turns of the nuts on the three threaded rods.

Despite these differences between the predicted and measured transmissibility, the prototype validates the concept of using axially compressed beams for vibration isolation and provides a significant amount of confidence in the model. The frequency at which isolation begins (transmissibility < 0) shifts from about 143 Hz for the uncompressed beam to about 103 Hz for the fully compressed beam. Furthermore there was very good agreement between the model and the experimental data when the resonant peaks are matched. This agreement between model and test data suggests that the correct amount of damping is being captured. This conclusion can be made more confidently because the prototype is made of a single piece of material, minimizing the number of sources for losses that are not captured in the model. This is one of the advantages of using SLS for studies in vibration isolation. However, this agreement relies upon post-build parameter measurements. In the next section, we consider how to account for some of the SLS manufacturing variability when designing to performance targets.

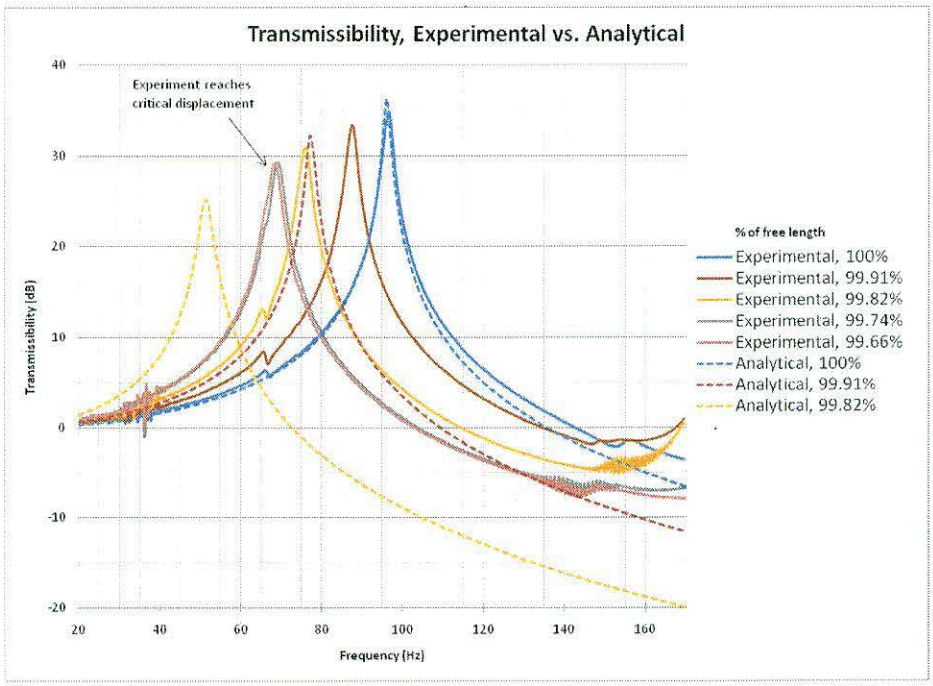

Figure 8. SLS Prototype Transmissibility Data and Analytical Prediction

4. Robust Design of Axially Compressed Beams for Vibration Isolation

A robust design process for using axially compressed beams for vibration isolation will need to consider how the manufacturing process introduces uncertainty into the transmissibility of the system. With the model developed in the previous sections, we can determine to what extent variation in the model parameters affects the transmissibility with a Monte Carlo simulation. Of particular interest is variation in the frequency at which the transmissibility transitions from positive to negative values (in decibels) for the lowest achievable beam stiffness. Another performance parameter of interest is the lowest achievable transmissibility at a particular frequency, which occurs with the lowest achievable beam stiffness. A Monte Carlo simulation can provide histograms of these performance parameters for specific sets of assumptions about the potential variations in the input parameters.

Based upon prototyping experiences with negative stiffness structures, fabricated with SLS and Nylon 11, the dimensions of a prototype were assumed to vary by as much as +/- 0.0005 m. The elastic and shear moduli for Nylon 11 were assumed to vary by as much as +/- 0.1 GPa. The density of Nylon 11 was assumed to vary by +/- 10%. Table 4 summarizes the assumed lower and upper bounds for the input parameters listed in the first column. Mean values for the parameters are identical to the pre-build design parameters listed in Table 1. Independent uniform distributions were assumed for each of the model parameters.

Table 4. Monte Carlo Input Parameters and their Variation

parameter	min	mean	max
E (MPa)	1.249×10^9	1.349×10^9	1.449×10^9
G (MPa)	3.964×10^8	4.964×10^8	5.964×10^8
ρ (kg/m^3)	878	975	1072
η	0.027	0.03	0.033
l (m)	0.1545	0.155	0.1555
w (m)	0.0075	0.008	0.0085
h (m)	0.002	0.0025	0.003
D (m)	0.0095	0.01	0.0105
d (m)	0.0028	0.0033	0.0038
N (coils)	7.328	7.414	7.500

Figure 9 shows the resulting histogram of 10,000 Monte Carlo simulations for the frequency at which the transmissibility transitions from positive to negative values for the lowest achievable beam stiffness. Figure 10 shows the resulting histogram of 10,000 Monte Carlo simulations for the transmissibility at a frequency of 114 Hz. 114 Hz is the frequency at which a zero axial load system is predicted to have zero transmissibility. The histograms are bimodal because the minimum achievable stiffness depends upon which buckling mode is the most limiting. For first-mode-buckling limited designs, the stiffness can be reduced to near zero and the transmissibility becomes negative at about 1 Hz, which explains the tall stack of designs with a frequency of about 1 Hz in Figure 9. These designs will perform the best and correspond to the cluster of normally distributed designs centered on about -45 dB in Figure 10. Second-mode-buckling limited designs will not be able to achieve quasi-zero stiffness as can be seen by the collection of designs that are distributed near 60 Hz in Figure 9. These designs will perform the worst and correspond to the cluster of designs with a minimum achievable transmissibility near -11 dB in Figure 11.

The Monte Carlo analysis has some important implications for the design of the negative stiffness structures. The analysis makes it apparent that the performance of a design is highly sensitive to manufacturing-induced variability. For example, if design requirements called for a minimum 40dB reduction in transmissibility at 114 Hz, only a first-mode-buckling limited structure would achieve the requirement. While there are many combinations of beam and spring dimensions and axial preload that satisfy this requirement in a deterministic sense, choosing designs with thicker beams (e.g., a beam height, h, with a mean value of 0.004 m, rather than the 0.0025 m specified in Table 4) increases the likelihood of first-mode buckling and satisfactory reductions in transmissibility.

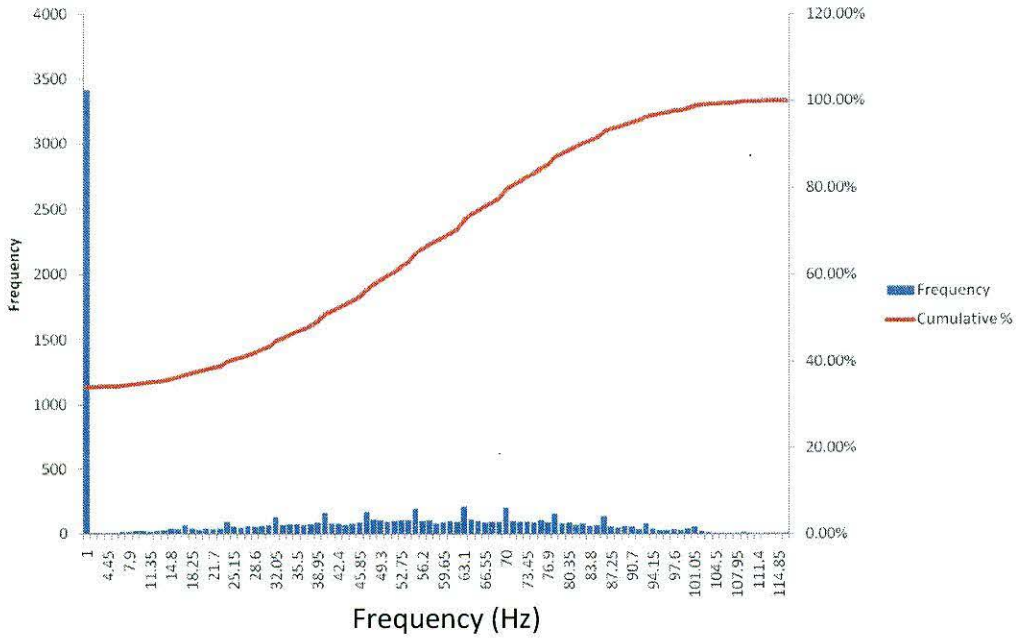

Figure 9. Minimum Achievable Frequency for Vibration Isolation

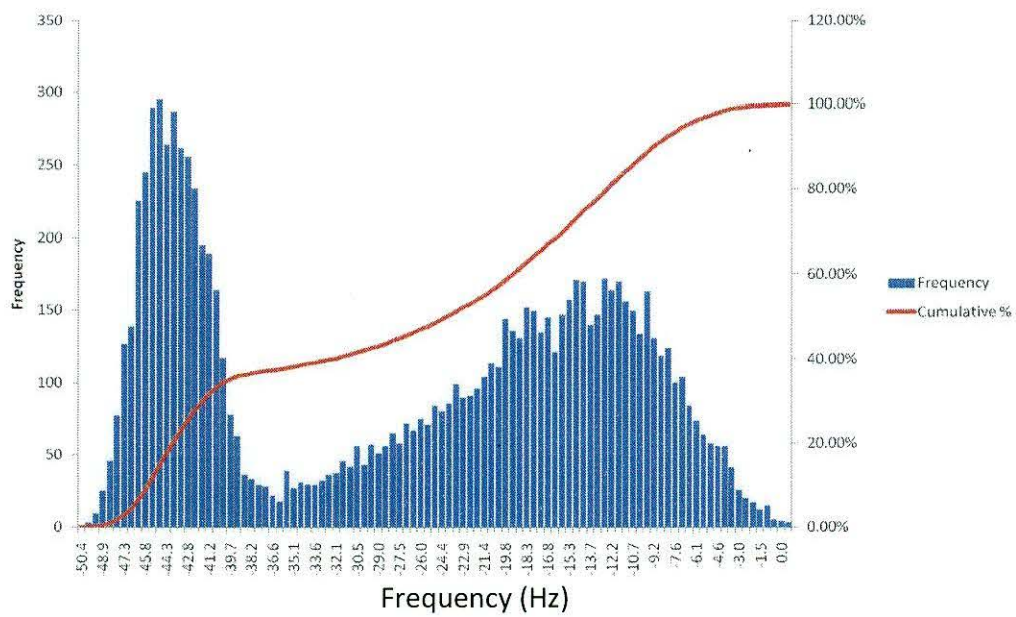

Figure 10. Minimum Achievable Transmissibility at 114 Hz

5. Discussion

In this paper we have laid the groundwork for a robust model-design-build-test process for negative stiffness structures comprised of axially compressed beams for vibration isolation. Building upon prior work (Kasdan et al., 2011; Kashdan, 2010), the research reported in this paper provides a more thorough model of the static and dynamic behavior of the structure. The

model was validated by comparison with experimental data from an SLS prototype system, which provided confidence in the predictive ability of the model but also highlighted the influence of manufacturing-induced variability on observed vibration isolation capabilities. Monte Carlo analysis was used to quantify the impact of typical, manufacturing-induced variability on experimental performance. This final section summarizes the lessons learned from this model-design-build-test cycle for improved agreement between predicted and observed behavior and improved vibration isolation performance.

To achieve better agreement between the model and the experiments, both the experimental procedure and the predictive models should be modified. During the experiments, the level of axial compressive strain in the beam needs to be known more precisely. Adding strain gages to the beam is a possible remedy. Also, measures need to be taken to prevent premature buckling. Specifically, the prototype buckled into the second mode much sooner than predicted by the model. The premature buckling into the second mode was probably encouraged by the helical spring providing a small moment at the beam's midpoint. This phenomenon could be avoided by redesigning the supporting spring; for example, by replacing the single spring with two concentric springs that attach to the beam symmetrically.

The model also needs to be improved to more accurately predict the initiation of buckling. For example, it is likely that the SLS process introduced additional geometric imperfections that were not captured in the Monte Carlo analysis. For example, building the beam horizontally in the build chamber could introduce a very small amount of curvature in the beam from curling. Pre-curvature would predispose the beam to premature buckling. These types of geometric imperfections are not easily modeled and would probably require a Monte Carlo simulation of a finite element model with an assumed mechanism for introducing geometric imperfections and varying them between simulations. This advancement would significantly lengthen the robust design process however it may be necessary to predict and potentially design around more realistic limitations to the technology.

In addition to capturing other sources of uncertainty in the modeling process, the Monte Carlo simulation could more accurately quantify each source of uncertainty in the SLS process. The Monte Carlo simulation presented here assumed independent uniform distributions for each of the model's parameters. More research into the SLS process could lead to more accurate models of the distributions of each design variable, along with models of the correlations between parameters. For example, variability in many of the parameters could be correlated with part bed temperature.

The results of this model-design-build-test process indicate that improved vibration isolation at lower frequencies requires better management of the buckling limits of the beam. Future work will involve modifying the predictive models and experimental prototypes to improve this performance. Also, both parametric and topological optimization are being pursued to provide some guidance for improving the performance of these negative stiffness structures and scaling this technology for larger masses at lower frequencies.

Acknowledgments

The authors gratefully acknowledge support from the Applied Research Laboratories at the University of Texas at Austin and the DARPA Strategic Technology Office (HR0011-10-C-0125) under Dr. Aaron Lazarus. Any opinions, findings and conclusions or recommendations

expressed in this material are those of the authors and do not necessarily reflect the views of the sponsors.

References

Albuzhev, P., 1989, *Vibration Protection and Measuring Systems with Quasi-Zero Stiffness*, Hemisphere Publishing Company, USA.

Blake, R. E., 2010, "Basic Vibration Theory" in *Harris' Shock and Vibration Handbook*, 6th ed., edited by A. G. Piersol and T. L. Paez, McGraw-Hill Inc., New York, pp. 2.1-2.32.

Blevins, R. D., 1979, *Formulas for Natural Frequency and Mode Shape*, Van Nostrand Reinhold Company, New York.

Juvinall, R. C. and K. M. Marshek, 2000, *Fundamentals of Machine Component Design*, 3rd ed., John Wiley & Sons, Inc., New York.

Kashdan, L., C. C. Seepersad, M. Haberman and P. S. Wilson, 2011, "Design, Fabrication, and Evaluation of Negative Stiffness Elements using Selective Laser Sintering", *Rapid Prototyping Journal*, In Press.

Kashdan, L., 2010, *Evaluation of Negative Stiffness Elements for Enhanced Material Damping Capacity*, M.S. Thesis, Mechanical Engineering Department, The University of Texas at Austin, Austin, TX.

Timoshenko, S. P. and J. M. Gere, 1961, *Theory of Elastic Stability*, 2nd ed., McGraw-Hill Inc., New York.

Young, W. C., 1989, *Roark's Formulas for Stress and Strain*, 6th ed., McGraw-Hill Inc., New York.